**OPEN**

# Transition Metal Dichalcogenide Growth via Close Proximity Precursor Supply

Maria O'Brien[1,2], Niall McEvoy[2], Toby Hallam[2], Hye-Young Kim[2], Nina C. Berner[2], Damien Hanlon[2,3], Kangho Lee[2], Jonathan N. Coleman[2,3] & Georg S. Duesberg[1,2]

[1]School of Chemistry, Trinity College Dublin, Dublin 2, Ireland, [2]Centre for Research on Adaptive Nanostructures and Nanodevices (CRANN) and Advanced Materials and BioEngineering Research (AMBER) Centre, Trinity College Dublin, Dublin 2, Ireland, [3]School of Physics, Trinity College Dublin, Dublin 2, Ireland.

Reliable chemical vapour deposition (CVD) of transition metal dichalcogenides (TMDs) is currently a highly pressing research field, as numerous potential applications rely on the production of high quality films on a macroscopic scale. Here, we show the use of liquid phase exfoliated nanosheets and patterned sputter deposited layers as solid precursors for chemical vapour deposition. TMD monolayers were realized using a close proximity precursor supply in a CVD microreactor setup. A model describing the growth mechanism, which is capable of producing TMD monolayers on arbitrary substrates, is presented. Raman spectroscopy, photoluminescence, X-ray photoelectron spectroscopy, atomic force microscopy, transmission electron microscopy, scanning electron microscopy and electrical transport measurements reveal the high quality of the TMD samples produced. Furthermore, through patterning of the precursor supply, we achieve patterned growth of monolayer TMDs in defined locations, which could be adapted for the facile production of electronic device components.

Two dimensional (2D) materials have recently attracted significant attention due to their wide range of electrical and optical properties[1–5]. While much initial research focused on graphene[1,2,6], its lack of a band gap suggests that materials such as layered semiconducting transition metal dichalcogenides (TMDs) could be more suitable as active materials for the semiconductor industry. Layered TMDs are inorganic materials with the chemical formula $MX_2$ where M is a transition metal and X is a chalcogen and each layer consists of an X-M-X sandwich. Molybdenum and tungsten disulfide ($MoS_2$ and $WS_2$) have thus far been the most heavily studied members of the TMD family, with monolayers of these materials having reported room temperature mobilities of up to $\sim$200 cm$^2$ V$^{-1}$ s$^{-1}$ and $\sim$50 cm$^2$ V$^{-1}$ s$^{-1}$ respectively[7,8]. These mobilities, in combination with high on/off ratios, outline the promise these materials hold for future electronic and optoelectronic devices[7,9–11]. $MoS_2$ has also been suggested for use in biosensors[12], and in solar cells due to its high visible light absorption[13]. Monolayers of $WS_2$ and $MoS_2$ have previously been obtained via mechanical exfoliation,[3,4,7] which can give crystals of high quality but with low throughput, and chemical exfoliation[14], which can produce large amounts of monolayers but involves longer times and harsh chemical treatments. Sonication assisted liquid phase exfoliation has also been demonstrated to give large amounts of few-layer sheets[15–18] but these can vary both in thickness and lateral size. Large scale films have been obtained using "bottom-up" approaches, via sulfurization of metal oxide[19,20] or metal films[21–24], however films produced using these methods are typically polycrystalline. Recently there have been significant advances using chemical vapour deposition (CVD)[25–31] to produce high quality crystals; however reproducibility and consistency across a single sample remain an issue, as different sizes and densities of $MoS_2$ have been reported along the length of a growth substrate[32–37]. In addition, many reports of TMD production via CVD require excess amounts of oxide precursors, which can result in oxysulfate contaminants[26,38]. This suggests that a more universal and reproducible approach is necessary, that does not rely on the presence of excess oxides.

Here, we present the synthesis of TMD monolayers by utilizing a close proximity precursor supply of liquid phase exfoliated $MoO_3$ nanosheets. This was achieved by drop casting the nanosheets onto substrates, and then placing the growth substrates face down on top of them, as illustrated in Fig. 1(e) and (f). Liquid phase exfoliated materials form stable dispersions that can be used as inks for printing devices such as photodiodes[39] and photodetectors[40]. Here we demonstrate their potential for use as controllable solid CVD precursors. The microreactor setup can be reproduced in a variety of CVD systems due to the simplicity of the approach. Additionally, we demonstrate that this process can be adapted to synthesize patterned TMDs by pre-patterning the precursor layer.
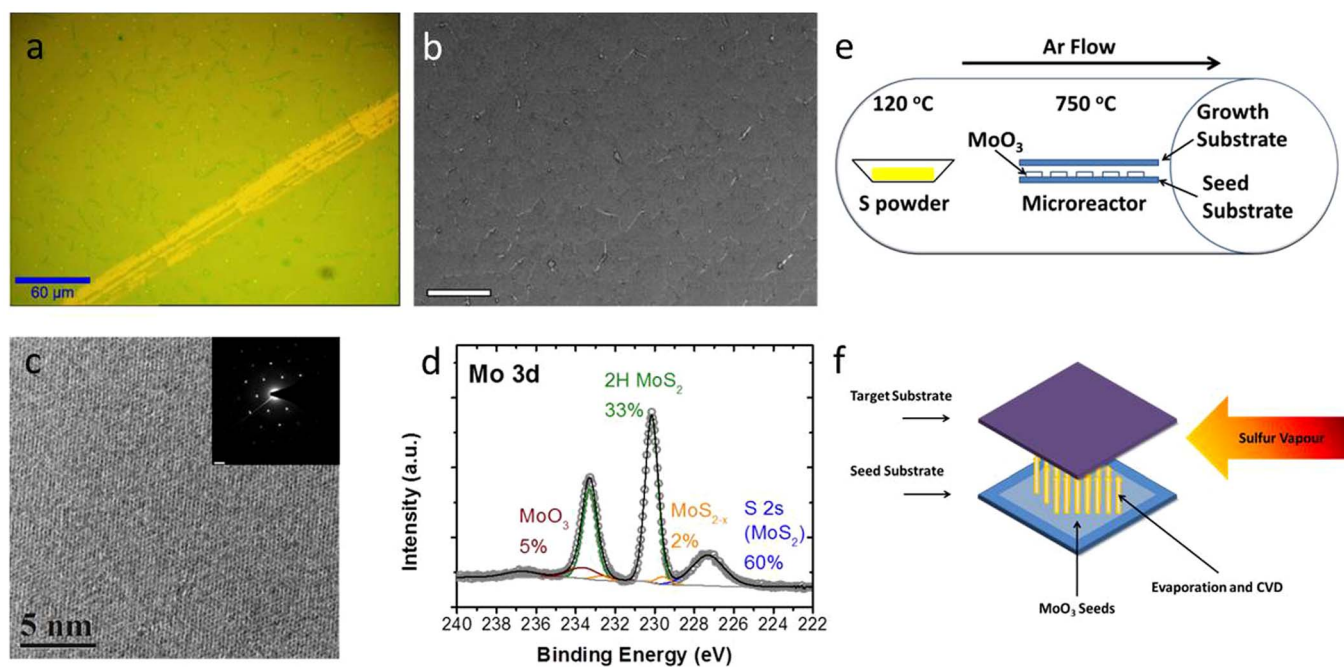
**Figure 1** | (a) Optical image of a polycrystalline $MoS_2$ continuous layer with minimal subsequent island growth on the terminated monolayer. A scratch has been introduced to show contrast with the underlying $SiO_2$ layer. (b) InLens SEM image showing the presence of grain boundaries. Scale bar is 2 μm. (c) HRTEM image of highly crystalline monolayer $MoS_2$, showing hexagonal crystal symmetry. Diffraction pattern inset further shows high quality and crystallinity of the monolayer. Scale bar for diffraction pattern is 2 $nm^{-1}$. (d) XPS spectrum of the Mo 3d core-level of a large area monolayer $MoS_2$ film. (e) Schematic of furnace setup. Sulfur powder is melted downstream and flowed through the microreactor (f) Schematic of CVD microreactor formed between the seed and target substrates, where sulfur reacts with $MoO_3$ nanosheets to form $MoS_2$ layers on the top substrate.

## Results

In Fig. 1(a) an optical image of a large scale $MoS_2$ monolayer film grown from $MoO_3$ seed nanoplatelets is shown. A scratch has been introduced here to allow contrast with the bare $SiO_2$ substrate underneath, emphasizing that the film is essentially homogenous over the visible area of approximately 300 × 250 μm. A typical scanning electron microscopy (SEM) image of an as-grown film is shown in Fig. 1(b). The visibility of grains and grain boundaries is clear using the topographically sensitive InLens detector, highlighting the homogeneity of the almost featureless surface over the depicted area of approximately 120 μm². The surface is predominantly flat and closed, with grain boundaries showing a slightly darker contrast. To investigate the crystal structure of the films, high resolution transmission electron microscopy (HRTEM) studies were undertaken. HRTEM, as shown in Fig. 1(c), revealed a perfect hexagonal lattice characteristic of highly crystalline $MoS_2$. This was confirmed by the hexagonal diffraction pattern obtained, shown in the inset of Fig. 1(c). A clearer, filtered version of the HRTEM image with measured lattice constants of 0.32 nm, in agreement with literature values, is available in Fig. S1 for reference.

A high resolution X-ray photoelectron spectroscopy (XPS) spectrum of the Mo 3d core-level region of the monolayer film is shown in Fig. 1(d). The position of the Mo $3d_{5/2}$ peak at ~230 eV is in agreement with the expected values for molybdenum in an oxidation state of $Mo^{4+}$, as is the case for $MoS_2$[41]. It should be noted that only very small amounts of sub-stoichiometric Mo[41] and $MoO_3$ were detected, indicating the high quality and uniformity of the studied areas. The S 2p core-level spectrum is shown in Fig. S2(b) and shows no observable edge-S[16], again confirming the predominantly monocrystalline nature of the films.

It has been reported that the intensity of photoluminescence (PL) in $MoS_2$ increases dramatically with decreasing layer number and that luminescence from a monolayer is the most prominent, while being absent in bulk material[4]. This is because the absence of inter-

layer coupling of electronic states at the Γ point of single layer $MoS_2$'s Brillouin zone[4] results in enhanced absorption and PL bands at a direct bandgap of ~1.8 eV, as opposed to an indirect bandgap of ~1.3 eV in the bulk[3,4]. This results in two resonances that have been well established to be direct excitonic transitions, known as the A1 and B1 excitons[4], at ~1.85 and 1.98 eV, respectively. Fig. 2(a) shows a magnified optical image of an area of $MoS_2$ monolayer over which PL and Raman maps were obtained. The average PL spectrum is shown in Fig. 2(c) with the relevant photoluminescence intensity map shown in Fig. 2(b). This map shows the emergence of PL peaks expected for monolayer $MoS_2$[3], verifying the high crystallinity and monolayer nature of the material. Raman spectroscopy was also used to evaluate the quality of the as-grown material. The $MoS_2$ Raman spectrum displays two characteristic Raman active modes, which in the case of a monolayer crystal are $E'$ at ~385 $cm^{-1}$, and $A'_1$ at ~403 $cm^{-1}$[42]. These arise from in-plane vibrations of Mo and S atoms and out-of-plane vibrations of S atoms in different directions only, respectively[42]. These peaks have been shown to shift in position with layer number[43], allowing monolayer $MoS_2$ to be identified easily and quickly. The maps of $E'$ in Fig. 2(d) and $A'_1$ in Fig. 2(e) show little variation in intensity over the entire area, apart from in the presence of grain boundaries. The average Raman spectrum for the scanned area in Fig. 2(f) shows peak positions of ~385 and 403 $cm^{-1}$ for $E'$ and $A'_1$, respectively for non-grain boundary areas[42,43], giving a separation of 18 $cm^{-1}$ as expected for monolayer $MoS_2$[42,43]. In the vicinity of the grain boundaries, both the $A'_1$ mode intensity and the peak separation of $E'$ and $A'_1$ decreases. This can be explained by correlating the Raman peak change to the PL map. The decrease in intensity at grain boundaries of the PL map suggests they are molybdenum rich, and therefore n-doped[36], quenching the photoluminescence. Previous reports show that n-doping results in softening of the $A'_1$ phonon, meaning a decrease of relative intensity and peak frequency difference between $E'$ and $A'_1$ Raman modes[44,45]. This implies that the grain boundaries shown here are n-doped, due to the decrease in $A'_1$
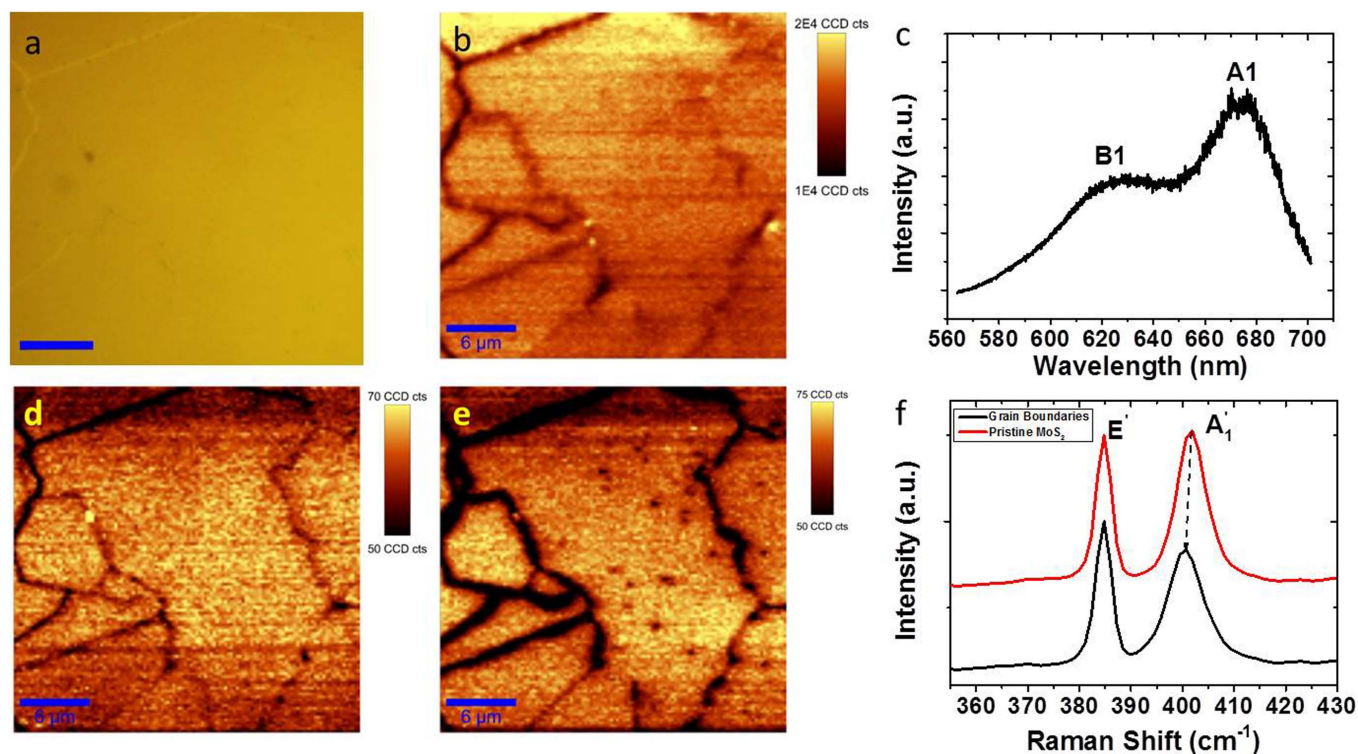
**Figure 2** | (a) Optical image of an MoS$_2$ film. Scale bar is 6 μm (b) Map of PL maximum intensity of the same area as in (a). The dark areas show a decrease in PL intensity in the vicinity of grain boundaries (c) Average PL spectrum over the scanned area of 14,400 individual point spectra. (d) Map of E' Raman peak maximum intensity (e) Map of A'$_1$ Raman peak maximum intensity (f) Average Raman spectra over grain boundary and non-grain boundary regions. Additional maps of this region and masks used to extract average spectra over grain boundary and non-grain boundary regions can be found in Section S5 of the Supporting Information.

peak intensity, the red shift in A'$_1$ peak position, and the localized decrease in PL intensity. Additional Raman and PL maps from this region can be found in Section S5 of the Supporting Information, along with the masks used to extract average spectra from grain boundary and non-grain boundary regions.

From the results presented above, as well as AFM data further on, it is evident that the films grown are of high quality, large area and are predominately monolayer, in agreement with some previous reports in the literature[46,47]. Previous reports of TMD production via CVD have relied on the presence of excess oxides, resulting in oxysulfate contaminants[26,38] and variation in growth along a sample[36,37]. The reason that predominantly closed, uniform monolayers are formed in the process presented here, and not in other growth setups, is that a close proximity precursor supply is used. This results in a microreactor being formed between the substrate with transition metal oxide precursor and the growth substrate which is placed face down on top of this, as depicted in Fig. 1(e) and (f). With this set-up, the precursor supply is homogenous over the whole growth area. This configuration is similar to setups that have previously been demonstrated for the growth of CVD graphene[48,49], with formation of large area single crystals of graphene attributed to an "improved" environment during growth[49]. It should be noted that an excess of sulfur is provided into the reaction chamber at elevated temperatures, making the oxide seed diffusion process the limiting step in this growth process.

The results can be explained by basic kinetic theory. Considering the MoO$_3$ precursor to be a solid state precursor in the form of a surface source, as illustrated in the schematic in the Supporting Information Fig. S4(a), it is clear that molecular vapour flow from a point source is directed towards a growth substrate according to a cosine distribution law, in a way analogous to Knudsen cells. A surface source can be considered to be a superposition of many point sources on a surface that combine to contribute to a vapour stream.

Here, the use of liquid phase exfoliated MoO$_3$ nanosheets dispersed in solution and drop cast onto a substrate as precursor can be assumed to be a superposition of many point sources, which therein forms a surface source. This uniformly delivers the precursor to the target growth substrate. The kinetic model for growth is presented in Section S4 in the supporting information. According to previous reports[46], and in agreement with the results here, the initial film nucleation occurs at the beginning of the growth process, as proven by unclosed areas with uniform triangle sizes, and starts from defects on the surface. These defects can be intrinsic to the growth surface or controlled by introducing seed molecules such as perylene-3,4,9,10-tetracarboxylic acid tetrapotassium (PTAS) or perylene-3,4,9,10-tetracarboxylic dianhydride (PTCDA) to seed growth[50]. Growth is thermodynamically favourable on these defect seeds, since shorter diffusion distances are needed[46]. The mean free diffusion length of incoming reactive species on SiO$_2$ is expected to be much shorter than that on MoS$_2$[46], meaning that growth will favourably occur laterally at the MoS$_2$ edges outwards until the substrate surface is fully covered by a monolayer of material, consistent with Frank–van der Merwe (FM) growth. This results, as shown in our experimental data, in atomically smooth, fully formed layers, as films can be seen with minimal subsequent layer growth.

Electrical transport measurements were performed across large channel areas that consisted of multiple grains. A field effect transistor was fabricated as described in section S3 of the Supporting Information. Fig. 3(a) shows drain current vs. drain voltage ($I_{ds}$ vs. $V_{ds}$) characteristics of the device from a two-terminal measurement with no applied back gate voltage, i.e. $V_{gs} = 0$ V. Slightly asymmetric contacts can be observed from the source-drain electrodes, which can be attributed to the presence of contact resistance. Fig. 3(b) shows the transfer characteristics ($I_{ds}$ vs $V_{gs}$) of the device for different source-drain voltages ranging from 0.5 to 2 V in increments of 0.5 V. The
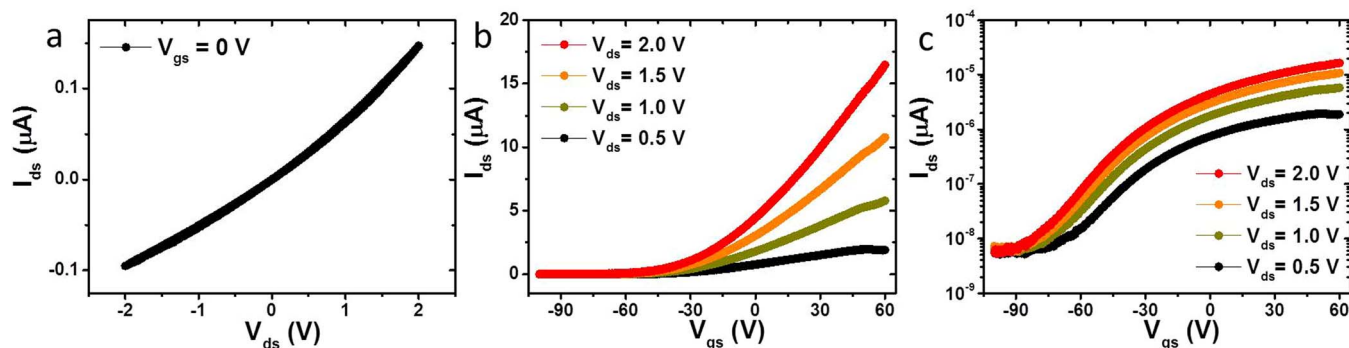
**Figure 3** | (a) Two terminal $I_{ds}$-$V_{ds}$ characteristics of the device for $V_{gs} = 0$. (b) Transfer characteristics ($I_{ds}$ vs $V_g$) of the device recorded for varying values of $V_{ds}$. (c) Transfer characteristics from (b) plotted on a logarithmic curve.

transfer curve shows strong n-type behaviour, and the current on/off ratio exceeds $10^3$ for all values of source-drain voltage. Furthermore, the off-state of the device has the same level for all the applied source-drain voltages, as shown in Fig. 3(c), meaning distinct on/off states can be observed. The field-effect mobility was estimated from equation (1):

$$\mu_{FE} = \frac{1}{C_{ox}} \cdot \frac{dI_{ds}}{dV_{ds}} \cdot \frac{L}{W} \cdot \frac{1}{V_{ds}} \qquad (1)$$

where $L$ is the channel length ($\sim 17.5$ μm), $W$ is the channel width ($\sim 145$ μm), $C_{ox}$ is the gate capacitance ($\sim 11.5$ nF), and $V_{ds}$ is the source-drain voltage. The maximum value of the slope, $dI_{ds}/dV_{ds}$, was used for calculations. For a bias voltage of 2 V, the field-effect mobility was estimated to be approximately 1.15 cm$^2$ V$^{-1}$ s$^{-1}$, which is in line with or superior to values previously reported for both CVD MoS$_2$[36,50,51] and mechanically exfoliated MoS$_2$, in the absence of high-k dielectric encapsulation layers[7,52]. This is an important result as it shows that large area CVD grown MoS$_2$ is potentially viable for electronic devices despite the presence of grain boundaries.

We have extended this growth procedure to the *in-situ* CVD patterning of MoS$_2$ by pre-patterning the MoO$_3$ seed layer before synthesis. This was done by sputtering MoO$_3$ layers through a patterned metal shadow mask. This results in patterns of MoS$_2$ monolayers that can be grown directly on a target substrate. The features demonstrated here are circles of closed MoS$_2$ films with a diameter of approximately 100 μm as shown in Fig. 4(a). The resulting patterns are of approximately the same diameter as the original square patterns, with some loss of square structure due to the initial spread of material during sputtering, and then the subsequent evaporation into a vapour source followed by re-deposition as MoS$_2$. This patterned growth is possible due to the close proximity of the oxide precursor. These patterned monolayers have the same high quality as the larger scale films as shown previously in Fig. 1(a). Although the resolution of the process is limited, as shown in Fig. 4(b), by a slight spread in growth, the method can produce multiple patterns without having to expose the monolayers to additional processing steps. This methodology could potentially be used to fabricate channels and other device components without the need for post growth processing steps.

Fig. 4(c) shows the area over which Raman and PL scans were taken. Fig. 4(d) and (e) show the corresponding respective intensity maps for the A1 and B1 exciton photoluminescence. The A1 intensity is far greater than B1 in all areas, further signifying the presence of highly crystalline monolayers[3]. Interestingly, there are small islands with enhanced PL that show no obvious change in the corresponding Raman maps. The average PL spectrum, as well as those from areas 1 and 2 as marked in Fig. 4(d), is shown in Fig. 4(f). One possible reason for this variation in PL intensity across the sample is that these patterned samples were synthesized using sputter deposited

MoO$_3$ samples. We hypothesize that these would not evaporate as readily as liquid phase dispersed MoO$_3$ nanosheets, as sputtered MoO$_3$ has been reported to form the sub-stoichiometric compound, MoO$_{3-x}$[53]. This could lead to inconsistencies in evaporation rate and therefore growth rate of monolayers, causing enhanced strain/doping to already grown monolayers as other growth begins to seed and join it. Raman analysis was used to evaluate the quality of the patterned CVD films. The maps of $E'$ in Fig. 4(g) and $A'_1$ in Fig. 4(h) show little variation in intensity over the entire area, apart from the presence of grain boundaries. The average Raman spectrum for the scanned area in Fig. 4(i) shows peak positions of $\sim$385 and 403 cm$^{-1}$ for $E'$ and $A'_1$, respectively[42,43], giving a separation of 18 cm$^{-1}$ as expected for monolayer MoS$_2$[42,43].

Having established patterned growth, it is worthwhile to discuss the effectiveness of grain boundary closure in the films, as it is possible to investigate the same features with atomic force microscopy (AFM) and Raman. In Fig. 4 below, we have shown selected area growth of 100 μm features. The AFM phase mode and topography mode imaging scans in Fig. 5(a) and (b), respectively show that the film is flat over the area of the scan, and consists of individual grains that grow together. The phase map, which would have better lateral resolution in samples of different material properties, shows a higher response in the vicinity of the grain boundaries, as seen by comparison with the optical image, while the topography map indicates all the grain boundaries are slightly elevated in comparison with the rest of the film. Various height profiles over raised grain boundaries, as indicated by the dark blue lines in Fig. 5(b), are shown in Fig. 5(c). The height in each case was observed to be $\sim$2.2 nm. This indicates that the areas shown are not gaps in the film, but rather buckled MoS$_2$ which forms as the grains grow together and upwards from different crystal lattice orientations. Similar features have previously been observed for CVD graphene[54,55]. The PL map in Fig. 4(d) also interestingly shows enhanced and diminished PL at different areas of the grain boundaries of the MoS$_2$ monolayers. Previous reports have linked an increase in PL intensity with p-doping[36] which suggests that these regions are sulfur rich. A decrease in PL intensity can similarly be attributed to n-doped molybdenum rich regions[36], as discussed previously, and in the Supporting Information, section S5. Future TEM investigations will be required to confirm this observation, and allow further analysis of the grain boundaries present in the as-grown materials. The grain boundary observations also confirm that the monolayer films are continuous, while possessing boundaries and defects similar to those observed in CVD grown graphene[56]. We further propose that Raman and PL mapping could act as a quick and viable method to identify and locate the grain boundaries of monolayer materials grown on a variety of substrates. We envisage that this methodology could be extended to other members of the TMD family, such as the transition metal diselenides, and other layered material sets by varying the precursors chosen. As a proof of principle, we have also demonstrated the growth of WS$_2$
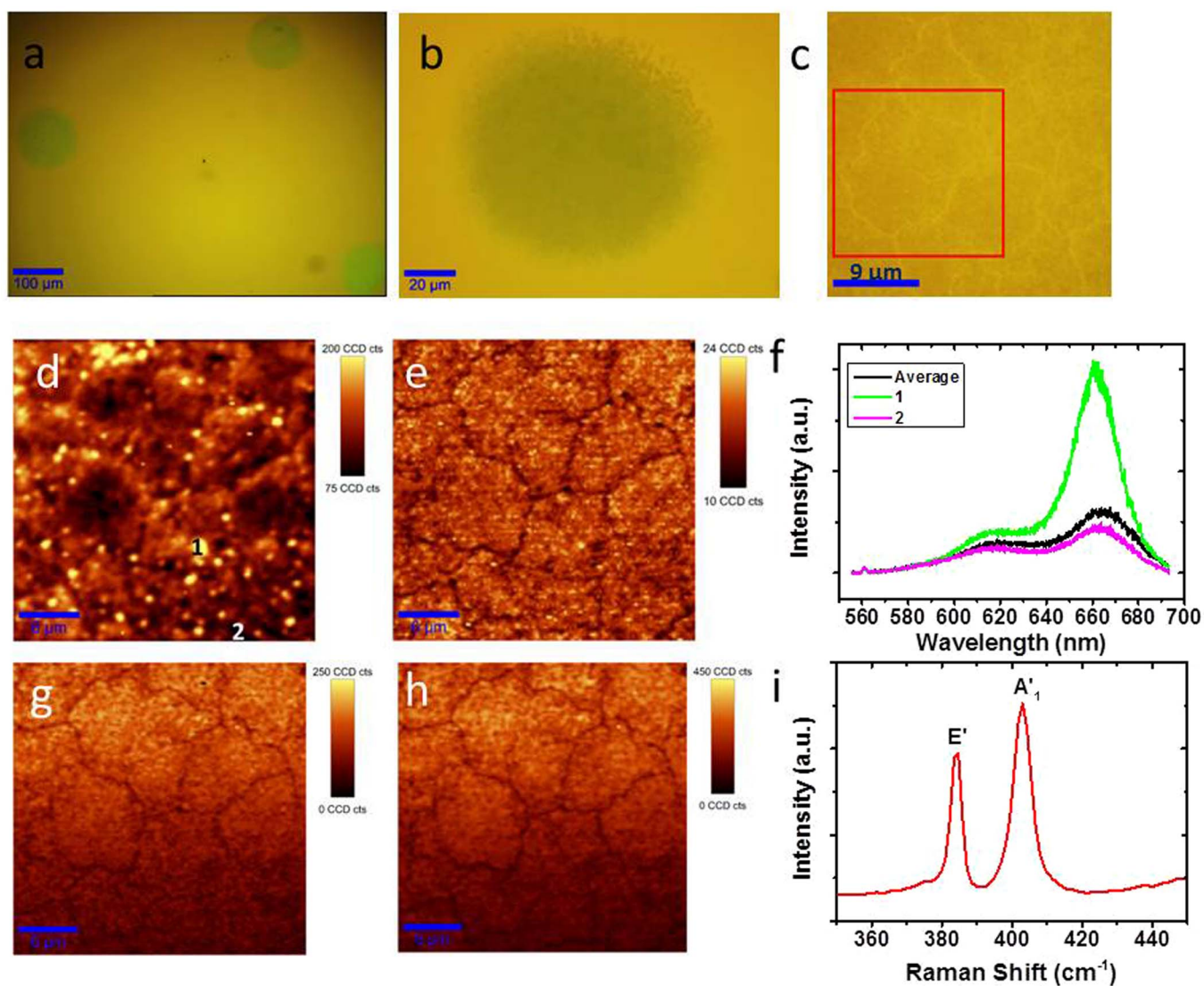
**Figure 4** | (a) Optical image of as-grown CVD monolayer $MoS_2$ dots (b) Optical image of a $MoS_2$ continuous layer grown by the pattern transfer technique with no observable subsequent island growth on the terminated monolayer. (c) Further enhanced magnification of the area shown in (b) over which Raman and PL scans were taken. Note that the Raman/PL maps are shown at an orientation of 90° to this area. The red box shows the area corresponding to AFM scans. Scale bar is 9 μm (d) A1 exciton maximum photoluminescence map (e) B1 exciton maximum photoluminescence map (f) photoluminescence spectra at points 1 and 2 as indicated in (d), and the average spectrum over the entire scanned area, consisting of 14,400 individual point spectra. (g) Map of $E'$ Raman peak sum (h) Map of $A'_1$ Raman peak sum. Scale bar is 6 μm for all Raman and PL maps. (i) Average Raman spectrum over 14,400 points taken in the scanned area the film, showing a peak separation of 18 cm$^{-1}$, which is in agreement with literature reports for monolayer $MoS_2$.
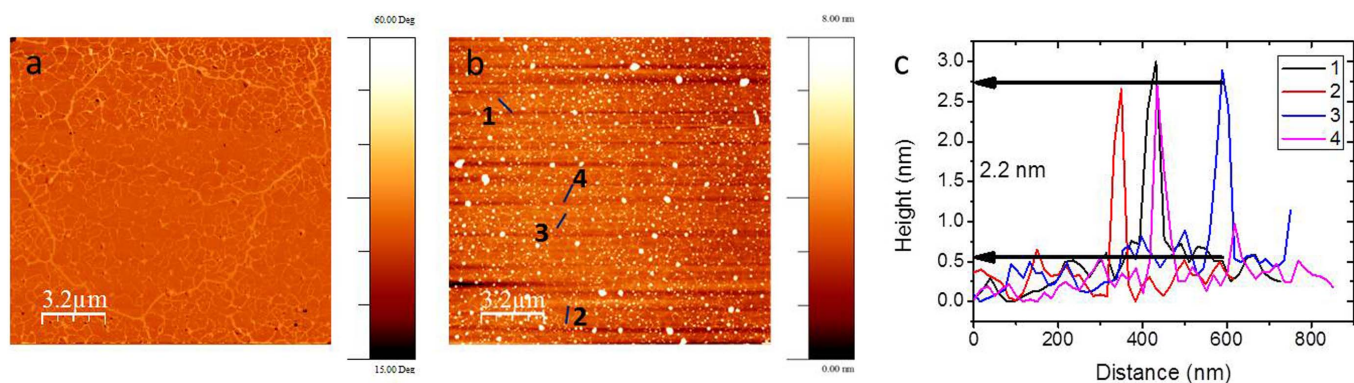


**Figure 5** | (a) Phase mode AFM image of the corresponding red box in Fig. 3(c). (b) Topography mode AFM image of the same area. (c) Height profiles over dark blue lines shown in (b).

monolayers using an analogous method, as shown in Section S6 of the Supporting Information, with similar high quality monolayers shown.

## Conclusions

We have presented a novel synthesis method for the production of TMD monolayers on arbitrary substrates by use of liquid phase exfoliated precursors in a close proximity microreactor setup for CVD growth. The high quality of the as-grown layers was shown using XPS, SEM and TEM. Raman and PL spectra were used to further probe the quality of the layers and the properties of the grain boundaries present. Electrical transport results showed carrier mobilities comparable to single crystal devices, indicating that the grain boundaries do not strongly deteriorate the electronic properties of the films. We outlined that this process can be extended to the growth of patternable TMD monolayers, by directly transferring patterns made with precursor layers to a growth substrate. This is an important result in the field of 2D materials, as, for the first time, it combines size-selectable, liquid dispersed nanosheets with chemical vapour deposition. This is a new pathway which could potentially lead to the development of patterned CVD monolayers for the production of future device components.

## Methods

**Large area growth from liquid phase exfoliated MoO₃.** Precursor layers of $MoO_3$ were made by dropcasting an IPA dispersion of $MoO_3$ nanoplatelets onto commercially available silicon dioxide ($SiO_2$, ~290 nm thick) substrates, which were thermally grown on top of <100> oriented crystalline silicon (Si) wafers. The dispersion of molybdenum trioxide ($MoO_3$) was liquid phase exfoliated, as described previously[57] and in full detail in the Supporting Information, Section S3. The wafers were then placed on a hot plate at 150°C until IPA had evaporated.

**Patterned synthesis.** $MoO_3$ patterns of 10 nm thickness were sputtered from a solid target (MaTecK GmBH) through a metal shadow mask, consisting of arrays of squares 100 μm in size, using a Gatan Precision Etching and Coating System (PECS). The patterns were deposited onto commercially available silicon dioxide ($SiO_2$, ~290 nm thick) substrates, which were thermally grown on top of <100> oriented crystalline Si wafers. The oxide deposition rate and thickness were monitored using a quartz crystal microbalance.

**Growth.** The $MoO_3$ seed films were placed face up in a ceramic boat with a blank $SiO_2$ on Si substrate face down on top of them, in order to direct growth onto the top, blank substrate. The boat was then placed into the centre of a quartz tube furnace. The samples were loaded into the hot zone which was heated to 750°C. Sulfur vapour was then produced by heating sulfur powder (MaTecK, 99%) to ~120°C in an independently controlled upstream heating zone of the furnace, and transported to the samples using Ar gas as carrier, for 20 minutes. A schematic of this is shown in Fig. 1(e). After sulfurization, the samples were annealed for 20 min at 750°C in Ar carrier gas, and then cooled down to room temperature. For TEM studies, the films were transferred to grids using a polymer support technique. Polymethyl methacrylate (PMMA 950K, MicroChem) was spin-coated onto the $MoS_2$, which were then floated on 2 M NaOH at room temperature until the $SiO_2$ layer between the $MoS_2$ and the Si substrates was completely etched away, leaving $MoS_2$/PMMA films floating on the surface[24]. After cleaning in deionized water the films were transferred onto 300 mesh lacey carbon copper TEM grids (Agar Scientific). The PMMA support layer was then dissolved in acetone at room temperature for 20 minutes.

**Analysis.** Raman spectroscopy and PL measurements were performed using a Witec alpha 300R with a 532 nm excitation laser and a laser power of <1 mW, in order to minimize sample damage. AFM measurements were carried out using a Veeco Dimension 3100 in tapping mode, with 40 N/m probes from Budget Sensors. SEM images were acquired using a Zeiss Ultra Plus SEM at an accelerating voltage of 1 kV. XPS was performed under ultra-high vacuum conditions ($<5 \times 10^{-10}$ mbar), using monochromated Al K$_\alpha$ X-rays (1486.6 eV) from an Omicron XM1000 MkII X-ray source and an Omicron EA125 energy analyzer. An Omicron CN10 electron flood gun was used for charge compensation and the binding energy scale was referenced to the adventitious carbon 1s core-level at 284.8 eV. The analyzer pass energy was set to 100 eV for the survey spectrum, and 15 eV for the Mo 3d and S 2p core-level spectrum. HRTEM analysis was performed in an FEI Titan transmission electron microscope at an acceleration voltage of 300 kV.

**Device Fabrication and Characterization.** The electrodes were patterned using electron beam lithography with PMMA A3 and subsequent evaporation of Ti/Au=10/30 nm contacts. The sample was annealed in a vacuum at 400 K for 140 minutes for removal of adsorbents[58]. Electrical characterization was carried out with a Keithley 2602 source meter unit and a Keithley 2400 source meter with JANIS probe station at room temperature under vacuum. The measurements were performed immediately after the annealing step without exposing the device to ambient conditions.

1. Geim, A. K. & Novoselov, K. S. The rise of graphene. *Nature materials* **6**, 183–191 (2007).
2. Novoselov, K. S. *et al.* Electric Field Effect in Atomically Thin Carbon Films. *Science* **306**, 666–669 (2004).
3. Mak, K. F., Lee, C., Hone, J., Shan, J. & Heinz, T. F. Atomically Thin MoS₂ :A New Direct-Gap Semiconductor. *Phys Rev Lett* **105**, 136805 (2010).
4. Splendiani, A. *et al.* Emerging photoluminescence in monolayer MoS₂. *Nano Lett* **10**, 1271–1275 (2010).
5. Mak, K. F., McGill, K. L., Park, J. & McEuen, P. L. The valley Hall effect in MoS₂ transistors. *Science* **344**, 1489–1492 (2014).
6. Schedin, F. *et al.* Detection of individual gas molecules adsorbed on graphene. *Nature materials* **6**, 652–655 (2007).
7. Radisavljevic, B., Radenovic, A., Brivio, J., Giacometti, V. & Kis, A. Single-layer MoS₂ transistors. *Nat. Nanotechnol.* **6**, 147–150 (2011).
8. Ovchinnikov, D., Allain, A., Huang, Y.-S., Dumcenco, D. & Kis, A. Electrical Transport Properties of Single-Layer WS₂. *ACS nano* **8**, 8174–8181 (2014).
9. Lembke, D. & Kis, A. Breakdown of High-Performance Monolayer MoS₂ Transistors. *ACS nano* **6**, 10070–10075 (2012).
10. Lopez-Sanchez, O. *et al.* Light Generation and Harvesting in a van der Waals Heterostructure. *ACS Nano* **8**, 3042–3048 (2014).
11. Lopez-Sanchez, O., Lembke, D., Kayci, M., Radenovic, A. & Kis, A. Ultrasensitive photodetectors based on monolayer MoS₂. *Nat. Nanotechnol.* **8**, 497–501 (2013).
12. Sarkar, D. *et al.* MoS₂ Field-Effect Transistor for Next-Generation Label-Free Biosensors. *ACS Nano* **8**, 3992–4003 (2014).
13. Tsai, M.-L. *et al.* Monolayer MoS₂ Heterojunction Solar Cells. *ACS Nano* **8**, 8317–8322 (2014).
14. Eda, G. *et al.* Photoluminescence from Chemically Exfoliated MoS₂. *Nano Letters* **11**, 5111–5116 (2011).
15. Coleman, J. N. *et al.* Two-Dimensional Nanosheets Produced by Liquid Exfoliation of Layered Materials. *Science* **331**, 568–571 (2011).
16. Backes, C. *et al.* Edge and confinement effects allow in situ measurement of size and thickness of liquid-exfoliated nanosheets. *Nat Commun* **5**, 4576 (2014).
17. Lee, K. *et al.* Electrical Characteristics of Molybdenum Disulfide Flakes Produced by Liquid Exfoliation. *Advanced Materials* **23**, 4178–4182 (2011).
18. Nicolosi, V., Chhowalla, M., Kanatzidis, M. G., Strano, M. S. & Coleman, J. N. Liquid Exfoliation of Layered Materials. *Science* **340** (2013).
19. O'Brien, M. *et al.* Plasma assisted synthesis of WS₂ for gas sensing applications. *Chemical Physics Letters* **615**, 6–10 (2014).
20. Lin, Y.-C. *et al.* Wafer-scale MoS₂ thin layers prepared by MoO₃ sulfurization. *Nanoscale* **4**, 6637–6641 (2012).
21. Kong, D. *et al.* Synthesis of MoS₂ and MoSe₂ films with vertically aligned layers. *Nano Lett* **13**, 1341–1347 (2013).
22. Gatensby, R. *et al.* Controlled Synthesis of Transition Metal Dichalcogenide Thin Films for Electronic Applications. *Appl Surf Sci* **297**, 139–146 (2014).
23. Lee, K., Gatensby, R., McEvoy, N., Hallam, T. & Duesberg, G. S. High-performance sensors based on molybdenum disulfide thin films. *Adv Mater* **25**, 6699–6702 (2013).
24. Yim, C. *et al.* Heterojunction Hybrid Devices from Vapor Phase Grown MoS₂. *Scientific reports* **4**, 5458 (2014).
25. Amani, M. *et al.* Electrical performance of monolayer MoS₂ field-effect transistors prepared by chemical vapor deposition. *Appl Phys Lett* **102**, 193107 (2013).
26. Lee, Y. H. *et al.* Synthesis of large-area MoS₂ atomic layers with chemical vapor deposition. *Adv Mater* **24**, 2320–2325 (2012).
27. Zhan, Y., Liu, Z., Najmaei, S., Ajayan, P. M. & Lou, J. Large-area vapor-phase growth and characterization of MoS₂ atomic layers on a SiO₂ substrate. *Small* **8**, 966–971 (2012).
28. Néstor, P.-L. *et al.* CVD-grown monolayered MoS₂ as an effective photosensor operating at low-voltage. *2D Materials* **1**, 011004 (2014).
29. Gutierrez, H. R. *et al.* Extraordinary Room-Temperature Photoluminescence in Triangular WS₂ Monolayers. *Nano Lett* **13**, 3447–3454 (2012).
30. Berkdemir, A. *et al.* Identification of individual and few layers of WS₂ using Raman Spectroscopy. *Scientific reports* **3**, 1755 (2013).
31. Elías, A. L. *et al.* Controlled Synthesis and Transfer of Large-Area WS₂ Sheets: From Single Layer to Few Layers. *ACS Nano* **7**, 5235–5242 (2013).
32. Liu, Y. *et al.* Mesoscale Imperfections in MoS₂ Atomic Layers Grown by a Vapor Transport Technique. *Nano Letters* **14**, 4682–4686 (2014).
33. Cheng, Y. *et al.* Van der Waals epitaxial growth of MoS₂ on SiO₂/Si by chemical vapor deposition. *RSC Advances* **3**, 17287–17293 (2013).
34. Ionescu, R. *et al.* Synthesis of Atomically Thin MoS₂ Triangles and Hexagrams and their Electrical Transport Properties. *IEEE Transactions on Nanotechnology* **13**, 749–754 (2014).
35. Ji, Q. *et al.* Epitaxial Monolayer MoS₂ on Mica with Novel Photoluminescence. *Nano Letters* **13**, 3870–3877 (2013).
36. van der Zande, A. M. *et al.* Grains and grain boundaries in highly crystalline monolayer molybdenum disulphide. *Nature materials* **12**, 554–561 (2013).
37. Ling, X. *et al.* Role of the Seeding Promoter in MoS₂ Growth by Chemical Vapor Deposition. *Nano Letters* **14**, 464–472 (2014).

38. Najmaei, S. *et al.* Vapour phase growth and grain boundary structure of molybdenum disulphide atomic layers. *Nature materials* **12**, 754–759 (2013).

39. Cunningham, G. *et al.* Photoconductivity of solution-processed $MoS_2$ films. *Journal of Materials Chemistry C* **1**, 6899–6904 (2013).

40. Finn, D. J. *et al.* Inkjet deposition of liquid-exfoliated graphene and $MoS_2$ nanosheets for printed device applications. *Journal of Materials Chemistry C* **2**, 925–932 (2014).

41. Baker, M. A., Gilmore, R., Lenardi, C. & Gissler, W. XPS investigation of preferential sputtering of S from $MoS_2$ and determination of MoSx stoichiometry from Mo and S peak positions. *Appl Surf Sci* **150**, 255–262 (1999).

42. Zhang, X. *et al.* Raman spectroscopy of shear and layer breathing modes in multilayer $MoS_2$. *Phys Rev B* **87**, 115413 (2013).

43. Li, H. *et al.* From Bulk to Monolayer $MoS_2$: Evolution of Raman Scattering. *Advanced Functional Materials* **22**, 1385–1390 (2012).

44. Chakraborty, B. *et al.* Symmetry-dependent phonon renormalization in monolayer $MoS_2$ transistor. *Phys Rev B* **85**, 161403 (2012).

45. Shi, Y. *et al.* Selective Decoration of Au Nanoparticles on Monolayer $MoS_2$ Single Crystals. *Scientific reports* **3**, 1839 (2013).

46. Zhang, J. *et al.* Scalable Growth of High-Quality Polycrystalline $MoS_2$ Monolayers on $SiO_2$ with Tunable Grain Sizes. *ACS Nano* **8**, 6024–6030 (2014).

47. Yu, Y. *et al.* Controlled Scalable Synthesis of Uniform, High-Quality Monolayer and Few-layer $MoS_2$ Films. *Scientific reports* **3**, 1866 (2013).

48. Chen, S. *et al.* Millimeter-Size Single-Crystal Graphene by Suppressing Evaporative Loss of Cu During Low Pressure Chemical Vapor Deposition. *Advanced Materials* **25**, 2062–2065 (2013).

49. Li, X. *et al.* Large-Area Graphene Single Crystals Grown by Low-Pressure Chemical Vapor Deposition of Methane on Copper. *Journal of the American Chemical Society* **133**, 2816–2819 (2011).

50. Lee, Y.-H. *et al.* Synthesis of Large-Area $MoS_2$ Atomic Layers with Chemical Vapor Deposition. *Advanced Materials* **24**, 2320–2325 (2012).

51. Zhan, Y. J., Liu, Z., Najmaei, S., Ajayan, P. M. & Lou, J. Large-Area Vapor-Phase Growth and Characterization of $MoS_2$ Atomic Layers on a $SiO_2$ Substrate. *Small* **8**, 966–971 (2012).

52. Qiu, H. *et al.* Electrical characterization of back-gated bi-layer $MoS_2$ field-effect transistors and the effect of ambient on their performances. *Appl Phys Lett* **100**, - (2012).

53. Werfel, F. & Minni, E. Photoemission study of the electronic structure of Mo and Mo oxides. *Journal of Physics C: Solid State Physics* **16**, 6091 (1983).

54. Muneer, A. *et al.* Nanoscale investigation of charge transport at the grain boundaries and wrinkles in graphene film. *Nanotechnology* **23**, 285705 (2012).

55. Duong, D. L. *et al.* Probing graphene grain boundaries with optical microscopy. *Nature* **490**, 235-239 (2012).

56. Huang, P. Y. *et al.* Grains and grain boundaries in single-layer graphene atomic patchwork quilts. *Nature* **469**, 389–392 (2011).

57. Hanlon, D. *et al.* Production of Molybdenum Trioxide Nanosheets by Liquid Exfoliation and Their Application in High-Performance Supercapacitors. *Chemistry of Materials* **26**, 1751–1763 (2014).

58. Schmidt, H. *et al.* Transport Properties of Monolayer $MoS_2$ Grown by Chemical Vapor Deposition. *Nano Letters* **14**, 1909–1913 (2014).

## Acknowledgments

## Author contributions

M.O. and G.S.D. conceived and designed the experiments and wrote the paper. M.O. synthesized materials by CVD. N.C.B., M.O. and N.M. carried out spectroscopic measurements and analysis. M.O. and N.M. performed electron microscopy. M.O. and T.H. performed AFM measurements and analysis. H.-Y.K. fabricated electrical devices, and H.-Y.K., T.H. and K.L. performed electrical measurements and analysis. D.H. and J.N.C. carried out liquid phase exfoliation and characterisation of nanosheets. G.S.D. supervised the whole project. All authors contributed to the discussion of the results and improvement of the manuscript.

## Additional information

**Supplementary information** accompanies this paper at http://www.nature.com/scientificreports

**Competing financial interests:** The authors declare no competing financial interests.

**How to cite this article:** O'Brien, M. *et al.* Transition Metal Dichalcogenide Growth via Close Proximity Precursor Supply. *Sci. Rep.* **4**, 7374; DOI:10.1038/srep07374 (2014).